Near-wall Thermometry Using Brownian Motion of PIV Particle Tracers

Kanjirakat Anoop
Mechanical Engineering Program
Texas A&M University at Qatar
Education City, Doha, Qatar
anoop.baby@qatar.tamu.edu

Reza Sadr
Mechanical Engineering Program
Texas A&M University at Qatar
Education City, Doha, Qatar
reza.sadr@qatar.tamu.edu

Abstract— **The present work reports an application of near-wall (on the order of 100 nm) thermometry utilizing Brownian motion of nano-particle image velocimetry (nPIV) tracer particles within a solid-fluid interface. Initially, a Monte Carlo simulation of Brownian particle movement in the evanescent wave region in the fluid-wall interface was employed to optimize the relevant measurement parameters. The results of the numerical simulation showed that the ratio of peak-width to peak-height of the nPIV correlation function could be successfully used as a temperature measurement index in the flow. Furthermore, the percentages of the particles remaining in the visible depth of the evanescent wave region may be considered as another thermometric parameter. Experimental studies using an objective-based evanescent wave technique were conducted to verify the results of the numerical simulations and to establish the experimental uncertainty of the temperature measurement. The experimental results verify the feasibility of temperature measurement within ±2.5°C accuracy bond and an out-of-plane resolution of O (100 nm) within the wall region. Variations of the evanescent wave thickness, i.e., out-of-plane resolution of thermometry, did not affect the sensitivity of the temperature measurement. However, the temperature range measured using the objective-based total internal reflection technique was limited due to changes in the optical characteristics of the imaging setup at higher temperatures.**

Keywords- Evanescent wave; Near-wall thermometry; nano-PIV; PIV.

I. INTRODUCTION

This paper is an extension of our previous work reported in ICQNM 2012 [1]. Temperature measurement, or thermometry, is of paramount significance in many industrial applications as well as in scientific research [2]. Recently, advancements in micro fabrication techniques have made it possible to miniaturize fluidic devices to the micro scale [3]. In this fluid transport regime, or microfluidics, fluid flows through small channels with overall dimensions on the order of 10 to 100 μm. Micro-heat exchangers, micro-mixers, polymerase chain reaction (PCR) microchips, microfluidic incubators, and Lab-on-a-chip devices are some examples of microfluidic applications. Microfluidic platforms are the main structure of the so-called Lab-on-a-chip systems that have helped to reduce not only the testing sample size but also the process time and component cost in biochemistry.

Thermometry at the microscale is an important requirement in the design and operation of micro-thermal devices for a wide range of applications, such as biological reactions, chemical processing fuel cells, and heat exchangers. [4]. Temperature-induced control of gene expressions and tumor metabolism, for example, requires accurate thermometry inside living cells for implementation [5]. Kucsko et al. [6] developed a nanometer-scale thermometry method in living cells utilizing the coherent manipulation of the electronic spin associated nitrogen-vacancy color centers in diamond. Temperature variations as small as 1.8 mK were detected using this technique. Chaudhari et al. [7] demonstrated the use of transient liquid crystal thermometry of micro fabricated PCR vessels for DNA replication. The reflected wavelengths of light from these excited liquid crystals are strongly dependent on the sample temperature. PCR processes require an accurate cycling of sample temperature, and the measurement of temperature uniformity in a micro-fabricated vessel array using encapsulated liquid crystal was demonstrated. Temperatures were measured with a resolution of ±0.5°C. Thermo-chromic liquid crystal–based slurries and paints have been reported to measure surface temperatures with a maximum spatial resolution of 1 μm [8].

Thermometry also plays a crucial role in electronic cooling inside miniaturized devices. In micro-electronic device systems, the exponential growth of component density has generated challenging thermal management issues for implementation. The present local chip heat fluxes are much higher for forced-air cooling techniques to effectively dissipate heat from the hotspots [9]. Single-phase forced-liquid and two-phase evaporative cooling techniques are currently designed for the microprocessors for better efficiencies. These cooling devices consist of mini or micro channels for maintaining a coolant flow through the microprocessors. Accurate measurements of the wall surface and bulk fluid temperatures would help to better estimate the heat transfer coefficients. Measurements with micron-scale spatial resolution without disturbing the flow would further assist in the better design of these channels.

With the available measurement methodologies, micro-scale thermometry techniques that can measure wall surface and bulk fluid temperatures can be broadly classified as invasive or non-invasive thermometry [2]. The invasive technique, for example, includes micro- or nano-thermocouples, resistance temperature detectors (RTD),

scanning thermal probes, and atomic force microscope (AFM) temperature probes. Non-invasive thermometry includes optical thermometry, liquid crystal thermometry, infrared thermometry, and Raman thermometry [10] .

Invasive, or contact-based, methods use standard CMOS (complementary metal-oxide semiconductor) technologies in the installation of conventional temperature sensors inside micro- or mini-channels. In small-scale applications, an array of diode sensors was used for surface temperature measurement at small scale [11]. However, the spatial resolution was relatively low because it depended on the dimensions of the diodes used. Additionally, this technique required intricate fabrication procedures for both the sensor array and the control unit. Han and Kim measured the surface temperature of a square area using a 32x32-diode array with a spatial resolution on the order of one hundred microns. Watanabe et al. [12] investigated the use of micro thermocouple probes for measuring cellular thermal responses. Williams and Wickramasinghe [13] introduced the concept of scanning thermal microscopy (SThM) by fabricating a 1000nm nm thermocouple at the end of a scanning tunneling microscope tip. The AFM-based thermal probe also works under similar principles [14]. Kim et al [15] used the SThM technique to measure temperature fields in a vacuum with a spatial resolution of 10 nm and a temperature resolution of 15 mK. The above measurement methods were not suitable for whole-field temperature measurement. In addition, these methods required electrical connections that could produce electromagnetic noise along with possible sparks. These effects could deter their use in corrosive environments. However, these sensors are intrusive, and their application can affect the micro-scale flow structure. Because of this limitation, non-invasive methods are generally preferred.

For the past few decades, many attempts have been made to measure the temperature field at the microscale with non-invasive or non-contact modes. Non-invasive thermometric methods such as molecular tagging thermometry (MTT), infrared thermometry (IRT), laser-induced fluorescence thermometry (LIFT) and particle image velocimetry (PIV)-based thermometry are generally preferred for micro-scale flow investigations [16-18]. Infrared thermography has been used to measure the surface temperature of microchannel heat sinks [19]. However, the emissivity values of the tested medium need to be known to accurately predict the temperature in this technique. LIFT is based on the temperature dependence of fluorescent dye intensity dissolved in the fluid and has been widely used in micro-fluidics thermometry. Ross et al. [20] demonstrated an application of the LIF method using a single dye and measured temperatures with a maximum uncertainty of 3.5°C. A two-color LIF method was suggested to overcome the uncertainties caused by possibly non-uniform illumination [21]. Rayleigh-Bernard convection was investigated using two-color laser-induced fluorescence by Sakakibara and Adrian [22]. Kim and Yoda [23] used a dual-tracer fluorescence thermometry technique at the microscale and showed a measurement uncertainty of ± 1.1°C at a spatial resolution of 3.7 µm in their work. Thompson and Maynes [24] utilized phosphorescence tracer dyes to simultaneously quantify fluid temperature and fluid velocity fields using MTT and molecular tagging velocimetry (MTV), respectively. Hu and Koochesfahani [25] conducted a simultaneous whole-field measurement of velocity and temperature using the MTT technique and were able to measure temperature with an uncertainty of 0.23°C.

Fluorescent particle tracers seeded in the fluid for micro- or nano-PIV are small and undergo Brownian motion [26] This motion can introduce a bias in PIV fluid velocity measurements at low velocity when using a cross-correlation method by increasing the width and reducing the height of the correlation peak. This is an undesirable effect in velocimetry as it reduces the signal-to-noise ratio of the results and increases the uncertainty of determining the average particle displacement. Olsen and Adrian [27] proposed that such spreading of the correlation peak width could be utilized for thermometry because the Brownian motion of the seeded particles has a direct dependence on the fluid temperature. Hohreiter et al. [28] demonstrated the use of a cross-correlation-based micro-PIV (µPIV) technique utilizing the Brownian motion of seeded particles to determine the temperature. Their results showed temperature measurement with an experimental accuracy of ± 3°C inside a microchannel. In a separate study, Chamarthy et al. [29] noted that a low image density PIV tracking method to process particle images performed better than the cross-correlation method for thermometry. The average difference between the predicted and measured fluid temperature was recorded to be ± 2.6°C with an out-of-plane resolution of approximately 20 µm.

Park et al. [30] showed the potential application of optical serial sectioning microscopy method (OSSM) for temperature measurement utilizing Brownian motion of nanoparticles in a fluid away from the wall. OSSM uses diffraction patterns of particle images to track its full three-dimensional Brownian motion. They used a dry objective lens to detect the diffraction patterns of 500 nm polystyrene fluorescent nanoparticles suspended in water at a low volume concentration of 4×10^{-6}. Their experiments for a fluid temperature range of 5 to 70°C showed a correlation between the Brownian diffusivity and the mean square displacement (MSN) of nanoparticles that could potentially be used in a non-intrusive and micro-scale thermometry for nanoparticle suspension fluids. However, in the near-wall region, the Brownian motion of nanoparticles is non-isotropic and hindered, and the estimated diffusion will not be same as that in the bulk flow. Moreover, in the micro-scale measurements discussed above, volume illumination is commonly used, which makes the measurements more complicated.

nPIV is an extension of µPIV, where illumination is provided only in the region very close to the wall on the order of O (100 nm) [31-36]. nPIV is based on evanescent-wave illumination created by the total internal reflection (TIR) of a laser beam at the fluid-solid interface. At the sub-micron scale, Brownian displacement is of the same length scale as that of the fluid convection and can therefore greatly affect fluid velocimetry when using particle tracers. The effect of hindered Brownian motion in the near-wall region is prominently visible in nPIV measurements as particles move

in and out of visible depth during the nPIV imaging time interval [36-38]. This movement could cause the cross-correlation peak-widths in nPIV measurements to behave in a different manner than that in µPIV measurements. We reported a simple numerical investigation of the effect of fluid temperature variation on the nPIV correlation function in the evanescent wave region in the near-wall region [1]. We showed that the PIV correlation function characteristics of the hindered Brownian motion of tracer particles in the near-wall region could be utilized for temperature measurements. However, the effect of the variation in fluorescence intensity of tracer particles and surface forces caused by the temperature change, which occurs in practical thermometry with fluorescence particles, were not considered.

The present work aims to extend and apply our earlier study [1] for near-wall temperature measurements, or nano-particle image thermometry (nPIT), to a wider temperature range and implement it in a real experimental setup. Prior to actual nPIV experimentation, the feasibility of the technique for non-intrusive near-wall temperature measurement is initially investigated using a Monte Carlo simulation to study the effect of temperature on the cross-correlation function peak-width and peak-height in the near-wall hindered Brownian motion. Artificial nPIV images are generated for fluids at stationary conditions and varying temperatures to include experimental effects such as non-uniform illumination, hindered Brownian motion, particle-wall surface forces, and temperature dependence of particle fluorescent intensity. Experiments are then performed under similar conditions to verify the results of the simulations and establish the applicability of nPIT and its experimental uncertainties and to demonstrate the practicability of using an objective-based nPIT setup for near-wall temperature measurement.

The remainder of this paper is organized as follows. In Section II the methods used in our analysis are described. Theoretical background for the thermometric method is also presented, and we describe our experimental setup and methodology used in the experimental measurements. The results are presented in Section III. Finally, we present our conclusions and ideas for future work in Section IV.

II. METHOD

A. Theoretical

As mentioned earlier, the nPIV method makes use of the evanescent wave generated at the glass-water interface to illuminate particles only in the near-wall region. Fig. 1 shows a schematic of the experimental setup for the present study. Here, the light beam passes through a microscope objective and microscope slide, with refractive index n_1 into the transparent fluid (water) with a lower refractive index, n_2, at an angle exceeding the critical angle, causing total internal reflection at the interface.

$$\theta_c = \sin^{-1}(n_2/n_1) \quad (1)$$

The electromagnetic field enters into the lower refractive index region and propagates parallel to the interface, creating an evanescent wave close to the interface. This evanescent wave excites the fluorescent particles in this region, while the particles further away in the bulk liquid remain unexcited. Intensity of the evanescent wave decays exponentially with distance normal to the wall (z),

$$I = I_o\, e^{\left(-\frac{z}{z_p}\right)} \quad . \quad (2)$$

I_0 is the maximum intensity at the wall and z_p is the penetration depth, given as:

$$z_p = \frac{\lambda_0}{4\pi n_1}\left[sin^2\theta - \left(\frac{n_2}{n_1}\right)^2\right]^{-\frac{1}{2}} . \quad (3)$$

Here λ_0 is the wavelength of the light and θ is the incident angle. For visible light at a glass-water interface, z_p is on the order of O (100 nm). However, the effective depth of the visible region z_v depends on the optical features of the imaging system: penetration depth, intensity of the incident laser beam, fluorescent particle properties, and characteristics of the imaging camera. In an actual experiment, z_v typically ranges from 300 to 400 nm. In an nPIV setup, the objective lenses generally have a larger focal depth than the penetration depth of the evanescent wave, and all of the particles in the image are in focus [36].

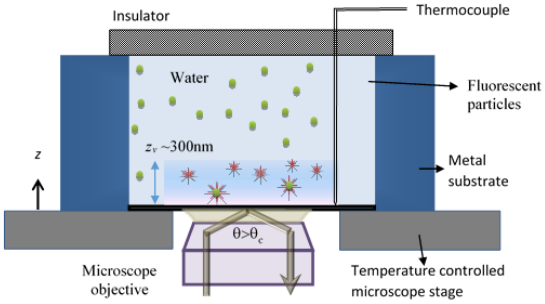

Figure 1: Schematic of nPIV measurement technique and the experimental setup used (not to scale)

For a stationary fluid, Brownian motion and surface forces govern the particle movement in the wall region. Brownian motion is usually characterized in terms of its diffusion coefficient. In an unconfined flow, the Stokes-Einstein equation represents the Brownian diffusion coefficient in the form given below [34].

$$D = \frac{kT}{6\pi\mu a} \quad (4)$$

Here k is the Boltzmann constant and T, a and μ are the temperature, diameter of particle and viscosity of the fluid, respectively. In addition to the direct dependence of the diffusion coefficient on temperature, the absolute viscosity of liquids also decreases with temperature. In the region close to the wall where nPIT is performed, the diffusion coefficient is hindered due to the additional hydrodynamic effects at the wall. The diffusion coefficient in this region is different from the value in Equation (1) and is different in the directions parallel and normal to the wall [34]. In the near-wall region,

where nPIT is interrogating, the diffusion coefficient is hindered due to the additional hydrodynamic effects at the wall and the Brownian diffusion coefficient, β, can be expressed in the tensor form as:

$$D = \begin{bmatrix} D_x & 0 & 0 \\ 0 & D_y & 0 \\ 0 & 0 & D_z \end{bmatrix} = \mathrm{D} \begin{bmatrix} \beta_{\parallel} & 0 & 0 \\ 0 & \beta_{\parallel} & 0 \\ 0 & 0 & \beta_{\perp} \end{bmatrix}. \quad (5)$$

$\beta_{\perp}$ and $\beta_{\parallel}$ are the wall correction factors for movement perpendicular and parallel to the wall, respectively [11]:

$$\beta_{\parallel} = \left[1 - \frac{9}{16}\left(\frac{a}{z}\right) + \frac{1}{8}\left(\frac{a}{z}\right)^3 - \frac{45}{256}\left(\frac{a}{z}\right)^4 - \frac{1}{16}\left(\frac{a}{z}\right)^5\right] \quad (6)$$

and

$$\beta_{\perp} = \left[\frac{2h \cdot (3h + a)}{6h^2 + 9ah + 2a^2}\right], \quad (7)$$

where a is the particle radius and $h=(z-a)$. As the particles move away from the wall, the correction factors tend to unity and the diffusion coefficient tends to that of the Stokes-Einstein value. In the present simulation, this anisotropic nature of Brownian diffusion coefficient is considered. Quantifying the relative changes in particle movement due to Brownian motion is the key principle used in nPIT. In the present simulation, this anisotropic nature of the Brownian diffusion coefficient is considered. Quantifying the relative changes in particle movement due to Brownian motion is the key principle used in nPIT. Details of the numerical simulation are presented next.

In the numerical simulation, particle displacement over a time period Δt due to Brownian motion $\Delta\vec{r} = \Delta x.\hat{\imath} + \Delta y.\hat{\jmath} + \Delta z.\hat{k}$ (where i, j, k are unit vectors in Car tesian co-ordinate system) is obtained from the Langevin equation [31, 35]. For a stationary fluid with no external forces acting on the particle, the Langevin equation in the direction parallel to the wall reduces to

$$\Delta x = \Delta y = \sum_{t=0}^{t=\Delta t} \{\chi \delta r\} \quad (8)$$

where χ is white noise and $\delta r = \sqrt{2D\delta t}$. Here, diffusion (D represents diffusion coefficient) is considered in the direction parallel to the wall. In the *z* direction perpendicular to the wall, the Langevin equation reduces to

$$\Delta z = \sum_{t=0}^{t=\Delta t} \left\{\frac{D_z}{kT} F_z \delta t + \frac{dD_z}{dz}\delta t + \chi \delta r\right\} \quad (9)$$

where D_z is the diffusion coefficient normal to the wall and t represents time. The presence of the wall has a significant effect on the distribution of particles in the near-wall region through surface-induced forces on the particles. The external forces (F_z) acting on the particles in the direction perpendicular to the wall include electrostatic (*el*) and van der Waals (*vdw*) forces caused by the presence of the wall as well as the buoyancy force (*b*). The sum of these forces results in a non-uniform particle distribution within the suspending medium in the wall region. The total force acting on a particle in the direction normal to the wall would be the summation of all of these forces, $Fz = F_{el} + F_{vdw} + F_b$, which generates a net repulsive force that pushes the tracers away from the wall.

From DLVO (Derjaguin, Landau, Vervey, and Overbeek) theory, the electrostatic repulsive force, F_{el}, is expressed as [39]

$$F_{el} = 4\pi\varepsilon_0\varepsilon a\left(\frac{kT}{e}\right)^2\left(\frac{\hat{\zeta}_p + 4\gamma_p \Psi a\kappa}{1 + \Psi a\kappa}\right)(4\gamma_w)\kappa e^{-\kappa(z-a)} \quad (10)$$

where $\kappa = 1/\lambda$, $\hat{\zeta}_p = e\zeta_p\,/kT$, $\hat{\zeta}_w = e\zeta_w\,/kT$,

$\gamma_p = \tanh(\hat{\zeta}_p/4), \gamma_w = \tanh(\hat{\zeta}_w/4), \Psi = (\hat{\zeta_p} - 4\gamma_p)/2\gamma_p^3$ and ε_0 is the vacuum electrostatic permeability. ε is the dielectric constant of the fluid, e is the elementary charge, λ is the wall's Debye length, and ζ_p and ζ_w are the zeta potentials of the particle and wall, respectively.

The van der Waals forces, F_{vdw}, can be expressed as [39]:

$$F_{vdw} = \frac{A}{6}\left[\frac{1}{(z-a)} - \frac{a}{(z-a)^2} - \frac{1}{(z+a)} - \frac{1}{(z+a)^2}\right] \quad (11)$$

where Hamaker's constant, A, is of order $O(10^{-20})$ for a spherical particle near a flat wall [33].

The buoyancy force acting on a particle suspended in a fluid is due to the difference in weight between the particle and the displaced fluid and is expressed as:

$$F_b = \frac{4\pi}{3}a^3 g(\rho_p - \rho_f) \quad (12)$$

where ρ_p and ρ_f are the particle and fluid densities, respectively, and g is the gravitational acceleration. This force is observed to be negligible when compared to the electrostatic and van der Waals forces. The effects of temperature on viscosity, Debye length, zeta potential [40], and the dielectric constant value of water [41] are also included in the simulation.

For Monte Carlo simulations, artificial images of tracer particles at time $t = 0$ and later at time $t = \Delta t$ are generated. Particle Brownian displacements in the *x*, *y*, and *z* directions are calculated for different time steps of $\Delta t = \sum\delta t$ using Equations (2) and (3) by including all the above-mentioned forces. The time step used in this work, $\delta t = 5\ \mu$s, is much smaller than Δt and is orders of magnitude larger than the particle momentum relaxation time [36]. Particle–wall collisions are considered perfectly elastic, preventing any particles from going 'through' the wall.

Particles were assumed to be circular with intensity values following a Gaussian distribution profile. The peak intensity values were selected from the experimental observations. In the present work, an illumination with exponential decaying intensity was considered in artificial images. The level of decay intensity was similar to the evanescent wave illumination in the described experiments. For a given optical setup undergoing total internal reflection,

the brightness (or size) of a particle in the image is an inverse function of its distance from the wall, where particles near the wall look bigger and brighter than those farther away. This variation in particle sizes in the field is created by implementing the exponentially decaying intensity of illumination normal to the wall combined with a fixed image noise level. An effective particle image diameter of four pixels with an airy disk pattern was employed for the brightest particle in the simulation.

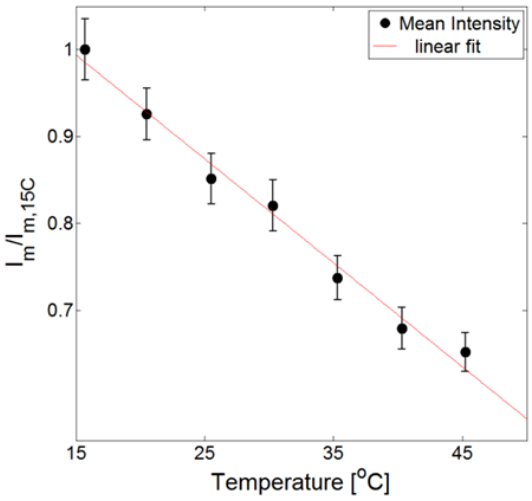

Figure 2: Variation of mean intensity of particles with temperature in experimental images

The excitation intensity of most fluorescent dyes varies with temperature. Initial experimental observations revealed that the mean particle intensity of the tracer beads also decreased with increasing temperature. Such variations can affect the PIT processing results to obtain temperature information from the obtained experimental images. The seeded particles used in this experiment were 100 nm (±5%) diameter polystyrene fluorescent particles (F8803, Invitrogen). Experiments were performed to quantify this effect, and Fig. 2 shows the results of the mean intensity of particles averaged over 100 images and normalized by their intensity at 15°C. This figure shows that the tracer particle intensity drops approximately 1.2 percent/°C for the temperature range tested. This effect is considered in the simulation of the generated nPIT images. Electronic noise and shot noise were also added to images using a combination of white and Gaussian distribution noise, respectively, to mimic real image characteristics [31].

A total of 1,200 particles with a radius of 50 nm were initially distributed over a distance of 875 nm normal to the wall in the fluid for the simulation. This resulted in a particle density of ~2.83 particles/μm^3 and an image size of (200x180 pixels (corresponding to 50μmx45μm), in the (x, y) directions, similar to the actual experimental images. Particles are initially uniformly distributed in the flow and then surface forces move the particles to their final steady state distribution. The final Probability Distribution Function (PDF) of the particles location throughout the visible region, z_v, at this stage is shown in Fig. 3 for two cases: a) with no surfaces forces, and b) with surface forces for ζ-potentials of $\zeta_{particle}$ = 100mV and ζ_{wall} = 80mV, respectively [35, 42]. The surface forces and zeta potential of the particles and surface contribute significantly to the distribution of particles near the wall. As the figure shows, when the surface force effects are considered, the particles are pushed away from the wall region, creating a sparse particle density near the walls. The probability distribution function of the particles, for a given surface force, can adequately be modeled by a Boltzmann profile for the steady state condition [35]

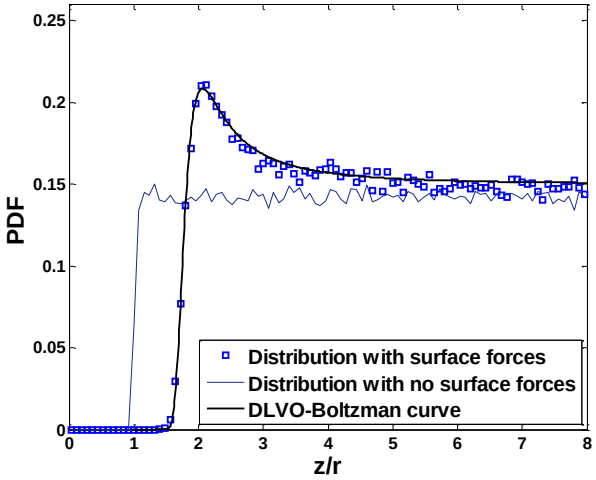

Figure 3: Probability distribution function of particle distribution throughout z_v

The image pairs were then processed using a standard FFT-based cross-correlation program to determine the width and height of the correlation peaks [31]. This program used a 3D Gaussian peak-finding algorithm based on a surface fit of 13 points in the peak region,

$$G(x,y) = A \cdot e^{\frac{-(x-x_0)}{2\sigma_x^2}} \times e^{\frac{-(y-y_0)}{2\sigma_y^2}}, \qquad (13)$$

where A is the peak height , σ_x and σ_y are representative peak widths in x and y directions, respectively. For a stationary fluid, the widths in both the x and y directions were similar in magnitude [29], therefore, the average peak-width value of x and y is presented.

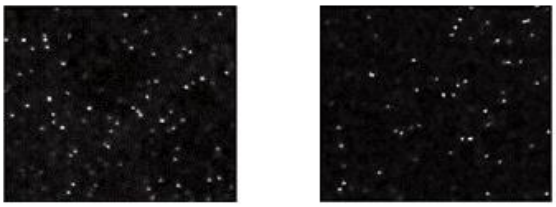

Figure 4: Typical experimental (left) and simulation (right) nPIT images

B. *Experimental setup*

An objective-based nPIV experimental setup [43] shown in Fig. 1 was used to obtain experimental images at a constant

fluid temperature. A constant temperature condition was achieved by placing a small fluid cell made of aluminum, the measurement cell, on top of a temperature-controlled inverted microscope stage. The measurement cell was made of an aluminum substrate with a glass coverslip (0.13 mm thick) pasted below it to provide optical access for the total internal reflection and imaging of the surface of the coverslip in the confined fluid. The fluid cell and microscope stage was insulated on the top. The microscope stage temperature and that of the fluid cell on it were maintained at a constant value by circulating water through the microscope stage from a constant-temperature supply tank (F25-ED Julabo). Prior to each experiment, the fluid was preheated to the temperature of the microscope stage to achieve a faster steady state condition. The fluid temperature in the fluid cell and in contact with the glass cover slip was recorded using precision K-type thermocouples. Experiments were conducted at a steady state condition where the fluid temperature was measured with an accuracy of ±0.1°C during each experiment.

The near-wall region was illuminated using an Ar-Ion continuous wave laser beam to excite the fluorescent particles. An EMCCD camera (ProEM 512, Princeton) attached to the microscope (Leica DMI6000B) captured images via a 63x1.47 NA oil immersion objective. The pixel resolution obtained from this imaging setup was 4,106 (pixels/meter). The seeded fluorescent particles had peak excitation and emission wavelengths of 505 nm and 515 nm, respectively. In all of experimental runs, the particle concentration was maintained at a constant volume fraction of 0.02%. Evanescent wave illumination was generated on the lower glass-water interface of the fluid cell with a laser beam incident angle of 63°. The depth of the visible region (z_v) was estimated to be z_v=350±25 nm based on the penetration depth (z_p of approximately 150 nm) and the intensity value of background noise in the captured images. Fig. 4 shows a typical experiment and simulated nPIT images obtained at 20°C.

For each experiment at varying fluid temperatures, 1,500 image pairs of 200x170 pixels were acquired with an inter-frame time delay of 1.6 ms. The interrogation window size was set to 180×150 pixels with a search radius of 20 pixels to ensure sufficient numbers of matched tracer particles in the interrogation windows. The images were then post-processed using the same cross-correlation program used in the simulation section to determine the correlation peak-widths and peak-heights.

III. RESULTS AND DISCUSSION

Equation (3) shows that Brownian displacement for a given fluid and particle size depends on the temperature and the inter-frame time delay Δt. Monte Carlo simulation was used to establish the effect of inter-frame time delay on PIV cross-correlation peak characteristics for different fluid temperatures. Synthetic images at different inter-frame time delays matching those of a typical nPIT experiment (1, 2, and 4 ms) were generated for the analysis. Image processing and analysis parameters were also kept equal to those used for experimental images.

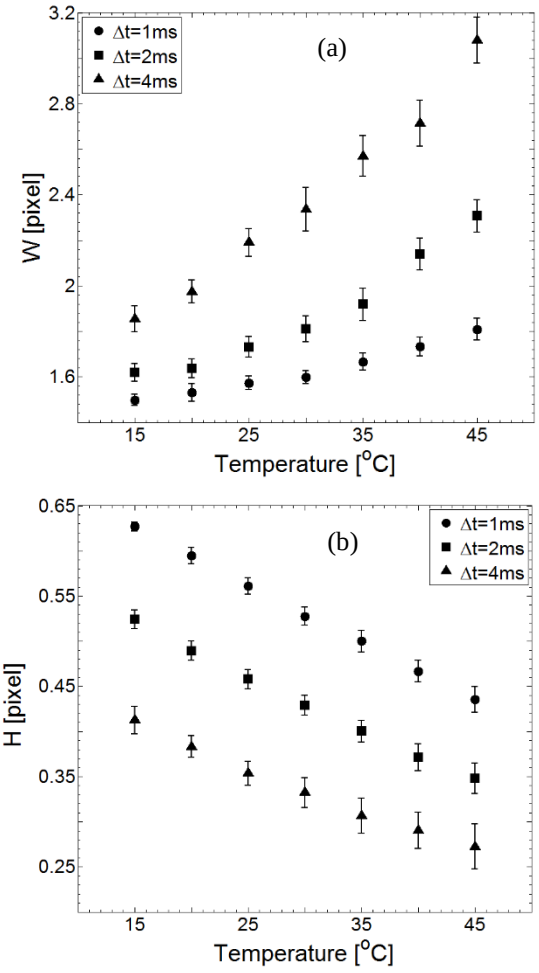

Figure 5: Peak-width variation with temperature (top) and peak-height variation (bottom) with temperature

Fig. 5a shows the variation of the calculated cross-correlation function peak-widths (W) for synthetic nPIT images for the three inter-frame time delays, with error bars representing 95% confidence intervals [44]. This figure shows a semi-linear increase in the width of the nPIT correlation function with temperature for all of the time delays considered. Fig. 5b shows the variation of the peak-height (H) with temperature for the same time delays given in Fig. 5a. The correlation peak value shows a decreasing trend with temperature due to the increase in Brownian motion of the particles. Fig. 5 shows that in addition to an increase in the magnitude of the error bars with temperature, the calculated uncertainty at a given temperature increases when the time delay increases from 1 ms to 4 ms. The increase in experimental uncertainty due to an increase in inter-frame time delay may be associated with levels of the tracer particle

mismatch caused by particle drop off due to Brownian motion [36].

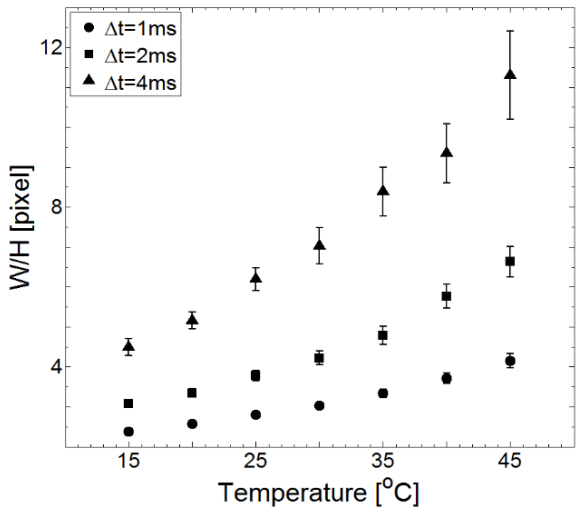

Figure 6: Variation of peak-width-to-height ratio with temperature obtained from the numerical simulation

Because the peak-width and peak-height variations seem to have opposite trends, the ratio of peak-width to peak-height is proposed as a better parameter for thermometry that offers a higher level of sensitivity than temperature measurement. The peak-width to peak-height ratio variation for various temperatures is depicted in Fig. 6. The temperature measurement sensitivity increases with increasing time delays, which can be attributed to a stronger effect of temperature on Brownian displacement of particle-tracers for longer time delays. However, measurement uncertainty also increases as the inter-frame time delay increases due to the deterioration of cross-correlation estimates. Considering additional experimental uncertainties, a smaller inter-frame time delay is preferable for an experiment, even though it has a slightly lower sensitivity to temperature variations.

After verifying the feasibility of using the nPIT technique based on Monte Carlo simulations, experiments were conducted to validate the results of the simulation. The nPIT images of the stationary fluid sample at varying bulk temperatures were collected using the objective-based illumination technique discussed earlier. Due to the small thickness of illumination in the evanescence region, Brownian motion caused the tracer particles to drop in and out of the visible region during the PIV inter-frame time delay Δt [36]. Because Brownian motion is a function of temperature, the number of particles staying in the visible region is expected to decrease with increasing fluid temperature.

Experimental images were analyzed to quantify this effect by measuring the percentage of the particles remaining within the visible depth (Ω) of the image, or "matched" particle, after a specified time delay Δt=1.6 ms. Fig. 7 depicts the percentage of particles that stayed within the visible region of z_v in an image pair, where error bars indicate a 95% confidence level of the presented data [44]. The experimental values are determined by searching for the particles in an image pair that stayed within a given observation window of five pixels. This figure shows that as the fluid temperature increased, the number of particles that stayed in the visible depth during the time interval decreased. This result is caused by an increase in Brownian motion at higher temperatures, pushing more particles out of the visible depth.

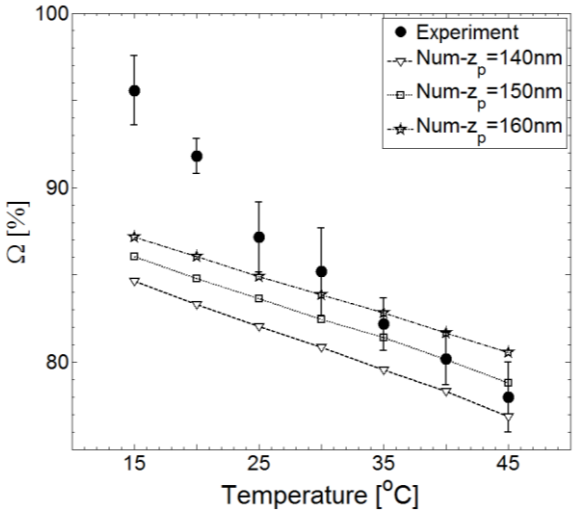

Figure 7: Percentage of particles remaining in the visible depth during nPIT experimentation

The results of the numerical simulation for the calculated values of Ω are also presented in Fig. 7 for three different evanescent wave thicknesses. Num-z_p in the figure represents the numerical prediction for the corresponding penetration depth. For these data, the number of the particles staying within the visible depth was determined based on the exact z position of the particles calculated from the numerical simulation. The numerical results also showed a systematic decreasing trend for the number of particles remaining in the visible region, confirming that this parameter could be used as an assessment tool in thermometry. This figure also shows that the percentage of particles remaining in the visible depth increases with increasing penetration depth of the evanescent wave, with similar decreasing trends with temperature increase. Fig. 7 shows that for a 30°C temperature increase, Ω predicts a 23% and 8% reduction for experimental and numerically estimated values, respectively. This difference may be attributed to other experimental factors, such as variations of particle size, fluorescence, and image noise with temperature, which affect detection of particles in the image. Further detailed experimental data are required to quantify this parameter as a tool for direct temperature measurement. In the present work, focus is given only to characterizing the effects of this particle "mismatch" on the standard cross-correlation function obtained from nPIT images for fluid thermometry. In an additional note, the above method also serves as a

metrological self-check on the basis of functional redundancy [45].

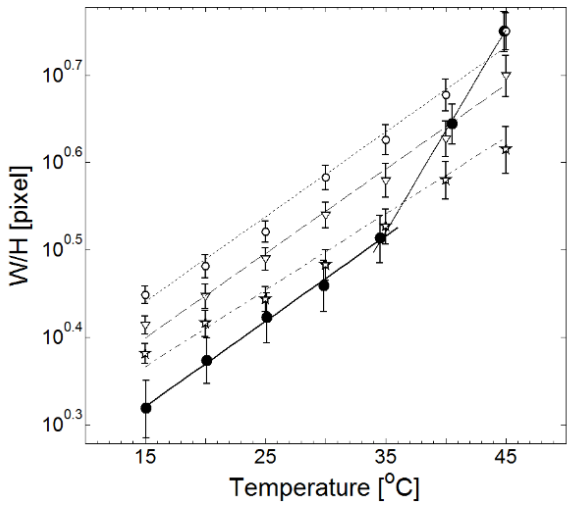

Figure 8: Correlation peak width-to-height ratio comparison for simulation and experiments at Δt=1.6 ms

Fig. 8 compares the peak-width to peak-height ratio obtained from the experiment for different temperatures at a Δt value of 1.6 ms and simulations performed at the same time delay on a semi-log plot. Numerical results are presented for three different penetration depths in the range of the estimated experimental depth. The temperature measurement sensitivity is not significantly influenced by the variation in penetration depth (or incident angle of TIR). The experimental data follows two trends: the initial slope of the data up to 35°C matches well with that of the simulations but deviates beyond 35°C. One reason for this deviation could be the change in optical characteristics of the objective used in the measurement, which was factory-corrected for working up to a temperature limit of 35°C. In addition, the optical properties of the contact oil used with the objective may also have varied at higher temperatures. These parameters could adversely affect measurements at higher temperatures and be cited as major drawbacks to the measurement technique using an objective-based system. There is a good agreement the between experimental and numerical trends for the peak-width to peak-height ratio for temperatures up to 35°C regardless of the assumed penetration depth. The ratio decreases with increasing penetration depth of the evanescent wave. At larger penetration depths, more particles remain in the visible region (imaged), resulting in higher correlation peak-height values. From the spread of uncertainty in the width-to-height ratio of the experimental data depicted in Fig. 8, the maximum uncertainty in the temperature measurement was estimated to be ±2.5°C for the case with z_v of approximately 350 nm.

The peak-width and peak-height values depend on the experimental and image processing parameters such as interrogation window size, number of particles, surface forces, and image noise level. Therefore, a calibration test to estimate the peak-width to peak-height ratio needs to be conducted prior to a practical near-wall temperature measurement.

IV. CONCLUSION

The feasibility of near-wall thermometry using evanescent wave illumination, or nano-particle image thermometry (nPIT), was investigated. Monte Carlo simulation was used to generate artificial nPIT images of the Brownian motion of fluorescent particle tracers in a stationary fluid with exponentially decaying illumination intensity from the wall. The results of simulations show that the cross-correlation peak-width increases while the peak-height decreases with increasing fluid temperature. The peak width-to-height ratio is determined to be the parameter of choice for quantifying temperature using the nPIT technique. Although higher temperature sensitivity was observed with larger inter-frame time delays, smaller time delays are preferred due to lower uncertainty values. Experiments were conducted, and the results were compared to the simulation results. The reduction in fluorescent intensity values with increasing temperature was observed to be significant and cannot be neglected in the Brownian-based thermometry using fluorescence particle tracers. The experimental results show a maximum uncertainty of ± 2.5°C in the temperature measurement with an out-of-plane measurement depth of approximately 350 nm from the wall. In addition, the objective-based near-wall thermometric method was imperfect at higher temperatures due to the changes in the optical characteristics of the imaging setup.

This work presents the application of Brownian motion analysis for near-wall thermometry in a stationary fluid. However, real applications often have fluid flow in the system. Detailed analysis for near-wall thermometry in the evanescent wave region together with velocimetry has not yet been reported. When there is no flow, the cross-correlation function (of image pairs) has similar widths in both the x and y directions. However, with the flow, the width in one direction of the flow will be different from the width perpendicular to it. The effect caused by the variation in temperature needs to be detected by further analyzing additional effects of the particle convection due to the fluid flow on the cross-correlation function [29]. In the future, we intend to conduct experimental studies on this aspect. In addition, in the present work fluorescent particles with a mean diameter of 100nm was only considered, as it was optimal for the measurement system. The effect of particle size distribution on near-wall thermometry was not investigated and would be an important factor to be considered for further studies.

ACKNOWLEDGMENT

This publication was made possible by NPRP grant # 08-574-2-239 and 9-1183-2-241 from the Qatar National Research Fund (a member of Qatar Foundation). The statements made herein are solely the responsibility of the authors.

REFERENCES

[1] K. Anoop and R. Sadr, "Evanescent wave-based near-wall thermometry utilizing Brownian motion," in *The Sixth International Conference on Quantum, nano and Micro Technologies*, Rome, Italy, 2012, pp. 12-17.

[2] P. Childs, J. Greenwood, and C. Long, "Review of temperature measurement," *Review of Scientific Instruments*, vol. 71, pp. 2959-2978, 2000.

[3] L. H. Fischer, G. S. Harms, and O. S. Wolfbeis, "Upconverting nanoparticles for nanoscale thermometry," *Angewandte Chemie International Edition*, vol. 50, pp. 4546-4551, 2011.

[4] M. M. Kim, A. Giry, M. Mastiani, G. O. Rodrigues, A. Reis, and P. Mandin, "Microscale thermometry: A review," *Microelectronic Engineering*, vol. 148, pp. 129-142, 2015.

[5] Y. Kamei, M. Suzuki, K. Watanabe, K. Fujimori, T. Kawasaki, T. Deguchi, Y. Yoneda, T. Todo, S. Takagi, and T. Funatsu, "Infrared laser–mediated gene induction in targeted single cells in vivo," *Nature methods*, vol. 6, pp. 79-81, 2009.

[6] G. Kucsko, P. Maurer, N. Y. Yao, M. Kubo, H. Noh, P. Lo, H. Park, and M. D. Lukin, "Nanometre-scale thermometry in a living cell," *Nature*, vol. 500, pp. 54-58, 2013.

[7] A. M. Chaudhari, T. M. Woudenberg, M. Albin, and K. E. Goodson, "Transient liquid crystal thermometry of microfabricated PCR vessel arrays," *Microelectromechanical Systems, Journal of*, vol. 7, pp. 345-355, 1998.

[8] T. Nozaki, T. Mochizuki, N. Kaji, and Y. Mori, "Application of liquid-crystal thermometry to drop temperature measurements," *Experiments in Fluids*, vol. 18, pp. 137-144, 1995.

[9] R. Mahajan, C.-p. Chiu, and G. Chrysler, "Cooling a microprocessor chip," *Proceedings of the IEEE*, vol. 94, pp. 1476-1486, 2006.

[10] K. L. Davis, K. L. K. Liu, M. Lanan, and M. D. Morris, "Spatially resolved temperature measurements in electrophoresis capillaries by Raman thermometry," *Analytical chemistry*, vol. 65, pp. 293-298, 1993.

[11] Y. M. Shwarts, V. Borblik, N. Kulish, E. Venger, and V. Sokolov, "Limiting characteristics of diode temperature sensors," *Sensors and Actuators A: Physical*, vol. 86, pp. 197-205, 2000.

[12] M. S. Watanabe, N. Kakutal, K. Mabuchi, and Y. Yamada, "Micro-thermocouple probe for measurement of cellular thermal responses," in *Engineering in Medicine and Biology Society, 2005. IEEE-EMBS 2005. 27th Annual International Conference of the*, 2005, pp. 4858-4861.

[13] C. C. Williams and H. K. Wickramasinghe, "Scanning thermal profiler," *Applied Physics Letters*, vol. 49, pp. 1587-1589, 1986.

[14] S. Gomès, A. Assy, and P.-O. Chapuis, "Scanning thermal microscopy: A review," *physica status solidi (a)*, vol. 212, pp. 477-494, 2015.

[15] K. Kim, W. Jeong, W. Lee, and P. Reddy, "Ultra-high vacuum scanning thermal microscopy for nanometer resolution quantitative thermometry," *Acs Nano*, vol. 6, pp. 4248-4257, 2012.

[16] P. Chamarthy, S. V. Garimella, and S. T. Wereley, "Measurement of the temperature non-uniformity in a microchannel heat sink using microscale laser-induced fluorescence," *International Journal of Heat and Mass Transfer*, vol. 53, pp. 3275-3283, 2010.

[17] S. Someya, D. Ochi, Y. Li, K. Tominaga, K. Ishii, and K. Okamoto, "Combined two-dimensional velocity and temperature measurements using a high-speed camera and luminescent particles," *Applied Physics B*, vol. 99, pp. 325-332, 2010.

[18] V. Natrajan and K. Christensen, "Two-color laser-induced fluorescent thermometry for microfluidic systems," *Measurement Science and Technology*, vol. 20, p. 015401, 2009.

[19] G. Hetsroni, A. Mosyak, and Z. Segal, "Nonuniform temperature distribution in electronic devices cooled by flow in parallel microchannels," *Components and Packaging Technologies, IEEE Transactions on*, vol. 24, pp. 16-23, 2001.

[20] D. Ross, M. Gaitan, and L. E. Locascio, "Temperature measurement in microfluidic systems using a temperature-dependent fluorescent dye," *Analytical chemistry*, vol. 73, pp. 4117-4123, 2001.

[21] M. Coolen, R. Kieft, C. Rindt, and A. Van Steenhoven, "Application of 2-D LIF temperature measurements in water using a Nd: YAG laser," *Experiments in Fluids*, vol. 27, pp. 420-426, 1999.

[22] J. Sakakibara and R. Adrian, "Whole field measurement of temperature in water using two-color laser induced fluorescence," *Experiments in Fluids*, vol. 26, pp. 7-15, 1999.

[23] M. Kim and M. Yoda, "Dual-tracer fluorescence thermometry measurements in a heated channel," *Experiments in Fluids*, vol. 49, pp. 257-266, 2010.

[24] S. Thomson and D. Maynes, "Spatially resolved temperature measurements in a liquid using laser induced phosphorescence," *Journal of fluids engineering*, vol. 123, pp. 293-302, 2001.

[25] H. Hu and M. M. Koochesfahani, "Molecular tagging velocimetry and thermometry and its application to the wake of a heated circular cylinder," *Measurement Science and Technology*, vol. 17, p. 1269, 2006.

[26] W. L. Cheng and R. Sadr, "Induced flow field of randomly moving nanoparticles: a statistical perspective," *Microfluidics and Nanofluidics*, vol. 18, pp. 1317-1328, 2015.

[27] M. G. Olsen and R. J. Adrian, "Brownian motion and correlation in particle image velocimetry," *Optics & Laser Technology*, vol. 32, pp. 621-627, 2000.

[28] V. Hohreiter, S. Wereley, M. Olsen, and J. Chung, "Cross-correlation analysis for temperature measurement," *Measurement Science and Technology*, vol. 13, p. 1072, 2002.

[29] P. Chamarthy, S. V. Garimella, and S. T. Wereley, "Non-intrusive temperature measurement using microscale visualization techniques," *Experiments in Fluids*, vol. 47, pp. 159-170, 2009.

[30] J. Park, C. Choi, and K. Kihm, "Temperature measurement for a nanoparticle suspension by detecting the Brownian motion using optical serial sectioning microscopy (OSSM)," *Measurement Science and Technology*, vol. 16, p. 1418, 2005.

[31] R. Sadr, K. Anoop, and R. Khader, "Effects of surface forces and non-uniform out-of-plane illumination on the accuracy of nPIV velocimetry," *Measurement Science and Technology*, vol. 23, p. 055303, 2012.

[32] K. Kihm, A. Banerjee, C. Choi, and T. Takagi, "Near-wall hindered Brownian diffusion of nanoparticles examined by three-dimensional ratiometric total internal reflection fluorescence microscopy (3-D R-TIRFM)," *Experiments in Fluids*, vol. 37, pp. 811-824, 2004.

[33] A. Banerjee and K. D. Kihm, "Experimental verification of near-wall hindered diffusion for the Brownian motion of nanoparticles using evanescent wave microscopy," *Physical Review E*, vol. 72, p. 042101, 2005.

[34] R. Sadr, C. Hohenegger, H. Li, P. J. Mucha, and M. Yoda, "Diffusion-induced bias in near-wall velocimetry," *Journal of fluid mechanics*, vol. 577, pp. 443-456, 2007.

[35] P. Huang, J. S. Guasto, and K. S. Breuer, "The effects of hindered mobility and depletion of particles in near-wall shear flows and the implications for nanovelocimetry," *Journal of fluid mechanics*, vol. 637, pp. 241-265, 2009.

[36] R. Sadr, H. Li, and M. Yoda, "Impact of hindered Brownian diffusion on the accuracy of particle-image velocimetry using evanescent-wave illumination," *Experiments in Fluids*, vol. 38, pp. 90-98, 2005.

[37] A. Goldman, R. G. Cox, and H. Brenner, "Slow viscous motion of a sphere parallel to a plane wall—I Motion through a quiescent fluid," *Chemical engineering science*, vol. 22, pp. 637-651, 1967.

[38] M. G. Olsen, "Depth of correlation reduction due to out-of-plane shear in microscopic particle image velocimetry," *Measurement Science and Technology*, vol. 21, p. 105406, 2010.

[39] M. R. Oberholzer, N. J. Wagner, and A. M. Lenhoff, "Grand canonical Brownian dynamics simulation of colloidal adsorption," *The Journal of chemical physics*, vol. 107, pp. 9157-9167, 1997.

[40] B. J. Kirby and E. F. Hasselbrink, "Zeta potential of microfluidic substrates: 1. Theory, experimental techniques, and effects on separations," *Electrophoresis*, vol. 25, pp. 187-202, 2004.

[41] M. Uematsu and E. Frank, "Static dielectric constant of water and steam," *Journal of Physical and Chemical Reference Data*, vol. 9, pp. 1291-1306, 1980.

[42] J. A. Fagan, P. J. Sides, and D. C. Prieve, "Calculation of ac electric field effects on the average height of a charged colloid: Effects of electrophoretic and Brownian motions," *Langmuir*, vol. 19, pp. 6627-6632, 2003.

[43] K. Anoop and R. Sadr, "nPIV velocity measurement of nanofluids in the near-wall region of a microchannel," *Nanoscale Research Letters*, vol. 7, pp. 1-8, 2012.

[44] L. Benedict and R. Gould, "Towards better uncertainty estimates for turbulence statistics," *Experiments in Fluids*, vol. 22, pp. 129-136, 1996.

[45] R. Taymanov and K. Sapozhnikova, "Metrological self-check and evolution of metrology," *Measurement*, vol. 43, pp. 869-877, 2010.